European Journal of Medicinal Chemistry 165 (2019) 1–10

Contents lists available at ScienceDirect

European Journal of Medicinal Chemistry

journal homepage: http://www.elsevier.com/locate/ejmech

Research paper

Design, synthesis and molecular docking studies of novel *N*-arylsulfonyl-benzimidazoles with anti *Trypanosoma cruzi activity*

Gisele E. Miana [a], Sergio R. Ribone [a], Domingo M.A. Vera [b], Manuel Sánchez-Moreno [c], María R. Mazzieri [a], Mario A. Quevedo [a, *]

[a] Departamento de Ciencias Farmacéuticas, Facultad de Ciencias Químicas, Universidad Nacional de Córdoba, Córdoba, Argentina
[b] Departamento de Química, Facultad de Ciencias Exactas y Naturales, Universidad Nacional de Mar Del Plata, Mar Del Plata, Buenos Aires, Argentina
[c] Departamento de Parasitología, Facultad de Ciencias, Universidad de Granada, Granada, Spain

ARTICLE INFO

Article history:
Received 4 October 2018
Received in revised form
12 December 2018
Accepted 6 January 2019
Available online 7 January 2019

Keywords:
Chagas disease
Synthesis
Biological activity
N-Arylsulfonyl-benzimidazoles
Molecular modeling
Trypanosoma cruzi

ABSTRACT

Currently, only two drugs (i.e. benznidazole (BZN) and nifurtimox (NFX)) have been approved for the treatment of *Trypanosoma cruzi* (*Tc*) infection, the etiological agent causing Chagas disease. Since both drugs exhibit severe side effects, patients frequently abandon therapy, resulting in an inefficient pharmacotherapeutic treatment. In this context, there is an urgent need to develop new, safer and optimised anti-*Tc* agents. In this report, we present the synthesis and biological activity of 11 novel and 3 already reported N-arylsulfonyl-benzimidazole derivatives (NBSBZD,**1**–**14**) currently in development as potential anti-*Tc* compounds. These compounds were designed as part of a library of synthetic arylsulfonyl heterocycle derivatives constructed from privileged structures exhibiting drug-like properties. Based on bioactivity assays against *Tc*, (in both the extracellular and intracellular forms), we observed that 10 compounds exhibited bioactivity against the epimastigote form, while six of them exhibited activity against the amastigote counterpart. Also, the compounds showed less cytotoxicity compared to the reference drug BZN as measured in Vero cell culture. In order to elucidate the potential mechanism of action, metabolite excretion profiles studies were performed, and complemented with molecular modeling studies performed over known *Tc* druggable targets. Consistency was observed between experimental and theoretical findings, with metabolic profiles showing that compounds **1**, **2**, **9**, **12** and **14** interfered with the normal glycolysis cycle of *Tc*, while molecular modeling studies were able to establish a solid structure-activity relationship towards the inhibition of 6-phospho-1-fructokinase, a key enzyme involved in the parasite glycolytic cascade. Overall, the present study constitutes a multidisciplinary contribution to the development of new anti-Chagas compounds.

1. Introduction

Chagas disease (CD), or American trypanosomiasis, is caused by infection with the protozoan parasite *Trypanosoma cruzi (Tc)*. This illness, originally observed in rural areas of the Americas in the 20th century, changed its epidemiological pattern with progressive urbanisation and spread to other continents. Current estimates indicate that around 7 million people are infected with *Tc* worldwide, and mostly in the continental Latin American countries, with CD remaining as one of the main public-health problems, causing more than 7000 deaths per year and exposing the risk of infection to over 25 million people [1].

To date, only two drugs have been approved to treat *Tc* infection, namely benznidazole (BZN) and nifurtimox (NFX). The former constitutes the first-line treatment in most countries and exhibits higher efficacy in the acute phase of CD compared to the chronic stage [2,3]. Unfortunately, both drugs exhibit severe side effects, including anorexia and weight loss, nausea and vomiting, nervous excitation, insomnia, depression, convulsions, vertigo, headache, sleepiness, myalgia, arthralgia, loss of balance, disorientation, forgetfulness, paresthesia, adynamia, acoustic phenomena, peripheral neuropathies, gastralgia, mucosal oedema, hepatic intolerance and skin manifestations [4,5]. These effects lead to poor patient adherence to treatment, resulting not only in therapeutic failure, but also increased parasitic resistance [6]. In this context, there is an urgent need for action with regard to the design and

* Corresponding author.
E-mail address: alfredoq@fcq.unc.edu.ar (M.A. Quevedo).

https://doi.org/10.1016/j.ejmech.2019.01.013
0223-5234/

development of safe and efficient novel drug candidates to treat CD, that are effective against the *Tc* forms associated with the acute and chronic phases of the disease.

As part of a lead discovery research project ongoing in our research group [7–10], a library of arylsulfonyl derivatives containing bioactive heterocyclic compounds (BSHet) was designed and prepared. The approach was based on *fragment drug design* (FDD) strategies aimed to combine privileged structures (scaffolds) in order to develop new bioactive compounds. This methodology has demonstrated to be very successful in the context of other drug discovery campaigns [11]. As part of our previous research efforts, the BSHet library was subjected to high throughput screening (HTS) assays over *Leishmania donovani, Plasmodium falciparum* and *Tc* at the *Head Parasite Chemotherapy, Swiss Tropical Institute*, Basel, Switzerland [7–10], with seven compounds exhibiting an IC_{50} against *Tc* below 6 mM, and three of them being identified as promising lead compounds for further optimisation based on their activity-toxicity profiles [10]. Furthermore, a family of BS-benzotriazole derivatives was evaluated using the epimastigote and trypomastigote forms of *Tc*, resulting in good inhibition of their growth [9].

In line with our previous research efforts, we herein report the synthesis and biological activity evaluation against *Tc* of a serie of BSHet, comprising 11 new and 3 already reported compounds, containing a combination of benzimidazole (BZD) and substituted benzenesulfonyl (BS) scaffold, which were termed N-arylsulfonyl-benzimidazole (NBSBZD, **1**–**14**, Fig. 1) derivatives. The BZD scaffold is present in compounds exhibiting diverse pharmacological activities [11], such as antiproliferative and antimicrobial properties, including anti-HIV, antioxidant, cysticidal, antiprotozoal, anti-helmintic, analgesic, antihypertensive, antiinflammatory, antipsychotic, anticoagulant and antidiabetic activity [12–14]. In addition, the BS scaffold is also present in chemical entities with diverse bioactivities, such as antibacterial and antileprotic effects, mostly derived from its well described PABA antagonism [15,16]. Also, the BS constitutes a very promising privileged scaffold able to enhance the bioactivity of other heterocycles, leading to analogues displaying similar or improved biological activities compared to their precursors [17–22].

In addition to the chemical synthesis, the 2D structural characterization and *in vitro* bioactivity against *Tc* is reported for the novel series of NBSBZD. Also, to shed light on their potential mechanism of action, bioactivity assays were complemented with profiling the glucose metabolism of *Tc* parasites exposed to these novel compounds. Finally, in order to study at the molecular level the potential mechanism of antitrypanosomal activity, molecular modeling techniques were used to describe the pharmacodynamic behaviour of the studied compounds against druggable targets of *Tc*.

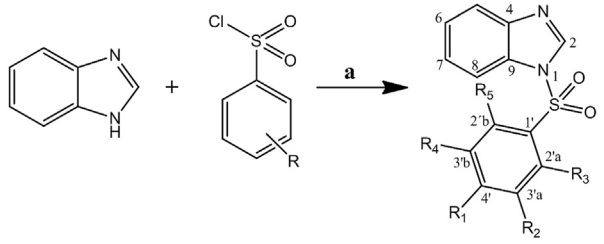

Compound	R_1	R_2	R_3	R_4	R_5
1	H	H	H	H	H
2	$NHCOCH_3$	H	H	H	H
3	$COCH_3$	H	H	H	H
4	CH_3	H	H	H	H
5	F	H	H	H	H
6	Cl	H	H	H	H
7	Br	H	H	H	H
8	H	H	NO_2	H	H
9	H	NO_2	H	H	H
10	NO_2	H	H	H	H
11	H	CF_3	H	H	H
12	CF_3	H	H	H	H
13	$C(CH_3)_3$	H	H	H	H
14	H	CH_3	CH_3	CH_3	CH_3

Fig. 1. General structure and synthesis of the studied NBSBZD (**1-14**). a) Reagents and conditions: methylene chloride, anhydrous pyridine, 25 °C.

2. Results and discussion

2.1. Drug-like properties of NBSBZD

Prior to our synthetic efforts, all compounds were evaluated as drug-like candidates by analysing their Lipinski parameters (Ro5) using the Molinspiration and OSIRIS Property Explorer software packages [23,24]. These analyses showed that all NBSBZD presented less than one violation of the rules corresponding to oral bioactivity. In particular, although compounds **11** and **12** exceeded the preferred number of halogens, they are classified as drug-like molecules. These results suggest adequate bioavailability for all derivatives. In addition, calculated LogP values predicted an appropriate lipophilicity range (2.42–4.97), while the topological surface area (TPSA) showed acceptable values (51.97–97.79 $Å^2$). Overall, both parameters are consistent with good membrane permeability (Table S1) [25]. In order to gain information regarding the potential toxicity and drug-likeness of the NBSBZD, OSIRIS Property Explorer software was also used [24], indicating that the $COCH_3$ and 2,3,5,6-CH_3 substituents on the BS scaffold elicited a more negative impact on the calculated toxicities, as well as in terms of the tumorigenic, irritant and reproductive effect than the rest of the functional groups (Table S2). It is worth mentioning that the fragments and the topology of the reference compounds (BZN and NFX) presented higher potential toxicity than the NBSBZD (Table S2). Finally, the drug-score and the drug-likeness calculated by the software showed positive values in all cases. (Table S2). Based on these preliminary studies, it was possible to conclude that the designed library of NBSBZD merited synthetic effort due to their drug like properties.

2.2. Synthetic procedures

The synthesis of **1**–**14** was carried out by applying a synthetic methodology previously developed in our research group [7–10]. Briefly, the synthesis of **1**–**14** was accomplished in one step by condensation of BZD with the corresponding arylsulfonyl chloride in methylene chloride under nitrogen atmosphere. All derivatives were obtained in good yields (71–100% of isolated products). All the compounds obtained constitutes novel chemical entities, with the exception of **1**, **4** and **13**, which have been previously reported by applying a different synthetic methodology [26,27].

Compounds **1**–**14** were fully characterized by means of HRMS, IR, ^1H NMR and ^{13}C NMR spectra (Figs. S1–S14), with their corresponding yields and melting points shown in Table S3.

2.3. Biological activity studies

2.3.1. In vitro activity assays

The series of NBSBZD was screened against the epimastigote form of *Tc* by applying *in vitro* assays, with selected compounds tested afterwards against the *Tc* amastigote form. [28,29] In addition, their unspecific cytotoxicity against Vero cells was also studied, with the corresponding values of biological activity, cytotoxicity and selectivity indexes (SI) being summarized in Table 1.

Table 1
In-vitro activity, toxicity and selectivity index (SI) determined for the BSBZD derivatives against the extracellular and intracellular forms of *Trypanosoma cruzi (Tc).*

Compounds	Activity IC_{50} (μM)[a]		Toxicity IC_{50} (μM)[b]	SI[c]	
	Epimastigote	Amastigote	Vero Cells	Epimastigote	Amastigote
BZN	15,8	23.3	13.6	0.8	0.6
1	9.0	37.3	1765.6	195.5 (244)	47.3 (78)
2	7.2	10.1	468.1	65.4 (82)	45.9 (76)
3	26.8	n.d	656.4	24.5 (31)	n.d
4	23.8	n.d	107.6	4.5 (6)	n.d
5	8.4	n.d	986.9	117.5 (147)	n.d
6	16.8	n.d	122.5	7.3 (9)	n.d
7	23.5	35.7	1188.0	50.5 (63)	33.3 (55)
8	5.5	n.d	120.1	22.0 (27)	n.d
9	4.6	15.9	647.7	141.1 (176)	40.6 (67)
10	2.6	n.d	346.7	135.4 (169)	n.d
11	13.9	n.d	59.8	4.3 (5)	n.d
12	6.2	24.0	459.8	74.8 (93)	19.2 (32)
13	3.0	n.d	68.5	22.5 (28)	n.d
14	2.2	19.0	205.3	91.7 (115)	10.8 (18)

Results are averages of three separate determinations.
n.d: not determined.
[a] IC_{50} = the concentration required to give 50% inhibition, calculated by using PROBIT® with (1, 10, 25, 50 and 100 μM).
[b] Measured towards Cell Vero after 72 h of culture.
[c] Selectivity index = IC_{50} Cell Vero/IC_{50} extracellular and intracellular form of parasite. In parenthesis: number of times that compound exceeded the SI reference drug (on extracellular and intracellular forms of *T. cruzi*).

Compounds **1**–**14** as well as the standard drug BZN were assayed at concentrations of 1, 10, 25 and 50 μM. All the activity determinations were carried out at the Department of Parasitology, University of Granada, by using the method reported by Sánchez Moreno et al. [30–32] As shown in Table 1, 10 out of the 14 compounds assayed exhibited a higher inhibitory potency than BZN against the epimastigote form of *Tc*. Remarkably, derivatives **8**, **9**, **10, 13** and **14**, were between three and five-fold more active than BZN. Clearly, the nature and position of the substituent on the BS group markedly affected the trypanocidal activity. Indeed, *p*-NO_2-NBSBZD (**10**), showed a two-fold increase in IC_{50}, relative to **8** and **9**, both of them bearing the nitro moiety in the *ortho* and *meta* positions, respectively. In line with this observation, the *p*-CF_3-NBSBZD (**12)** exhibited twice the potency of the *m*-CF_3 analogue **11**, while a fluorine atom on the *para* position of NBSBZD (**5**) also resulted in higher potencies compared to compounds containing *p*-Cl or *p*-Br substituents (**6** and **7**, respectively). The enhanced anti-*Tc* activity of compounds **13** (*p*-$C(CH_3)_3$-NBSBZD) and **14** (2,3,5,6-$(CH_3)_4$-NBSBZD) compared to **1**, could be attributed to the more bulky substituents of the former derivatives. On the other hand, compounds **3**, **4**, and **7** were less potent than BZN, but notably they were more selective for *Tc* (Table 1).

The activity against the intracellular parasite (amastigote form) was determined for selected compounds and based on the most promising ones after primary screening against epimastigote forms. Therefore, compounds **1**, **2**, **7**, **9**, **12** and **14** were assayed at the concentrations of 1, 10, 25 and 50 μM, with their IC_{50} values shown in Table 1. Noteworthy, compounds **2**, **9** and **14**, exhibited higher inhibitory potencies than the reference BZN, with **2** showing an almost two-fold increase in the inhibitory activity against the amastigote form of *Tc* and a 76-fold increase in the SI value.

2.3.2. Determination of metabolites excretion

It is well-known that trypanosomatids are unable to completely degrade glucose into CO_2 under aerobic conditions. Consequently, they excrete a considerable part of the hexose skeleton into the medium as partially oxidised fragments in the form of fermented metabolites. The nature and percentage of the partially oxidised fragments is dependent on the metabolic pathway involved for glucose biotransformation by each of the species considered [33]. In particular, *Tc* consumes glucose at a high rate, thereby acidifying the culture medium as a consequence of the incomplete oxidation to acids [33]. Usually, the final products of glucose catabolism in *Tc* are CO_2, succinate, acetate, D-lactate, pyruvate, and L-alanine [34]. Succinate is important because its main role is to maintain the glycosomal redox balance that facilitates the re-oxidation of NADH produced in the glycolytic pathway. Succinic fermentation has the advantage of requiring only half of the phosphoenolpyruvate produced to maintain the NAD+/NADH balance, while the remaining pyruvate is converted inside the mitochondrion and the cytosol into acetate, D-lactate or L-alanine, depending on the degradation pathway [35,36].

Taking into account that the NBSBZD presented in this work demonstrated good potential as new trypanocidal agents, and in order to further study if the bioactivity of the studied compounds is related to some extent of glucose metabolism modification, we studied the ^{1}H NMR spectra of the culture media corresponding to the *Tc* epimastigote form after treatment with **1**, **2**, **9**, **12** and **14**. In this way, the final excretion products were qualitatively and quantitatively identified (Fig. S15), and compared to those obtained from parasites maintained in drug-free medium (control) for 96 h. The presence of acetate, succinate, D-lactate and L-alanine was confirmed in the control experiments and, as expected, succinate and acetate were the most abundant end products identified. Remarkably, after treatment of the parasites with the selected NBSBZD, the excretion profiles of catabolites was substantially modified at the dosages assayed (Table 2), with each compound producing a particular metabolite excretion profile.

Table 2
Variation percentages in the height of the peaks corresponding to catabolites excreted by *Tc* epimastigotes in the presence of BSBZD derivatives at their IC25 compared to a control sample.

Metabolite/Compound	Succinate	Pyruvate	Acetate	L-Alanine	D-Lactate
1	−15,96%	−13,41%	3,31%	−3,24%	16,43%
2	28,33%	2,38%	12,30%	6,80%	25,52%
9	−33,16%	−30,20%	−16,60%	−22,73%	−3,97%
12	−7,22%	10,63%	11,76%	9,92%	25,78%
14	−7,22%	10,90%	11,97%	10,41%	26,43%

(−) and (+) = ^{1}H NMR peak intensity reduction and increase, respectively.

Based on the presented evidence, we hypothesised that the biological activity of the series of NBSBZD is mediated via interference with one or more enzymes participating in the glycolytic cycle. In order to further study this feature, molecular modeling techniques were used to study their inhibitory potential over previously reported therapeutic targets of *Tc*, with particular emphasis on those involved in the metabolism of glucose.

2.4. Virtual screening of Tc potential targets

2.4.1. Target search in databases

To initiate the screening of potential targets, the ChEMBL database from the European Bioinformatics Institute was explored [37], in order to compile available information regarding known *Tc* therapeutic targets. Results were clustered by protein ID, UniProt accession numbers [38], and the number of tested small molecule inhibitors with reported IC50 values (Table 3).

As can be seen, a total of 14 possible targets were found, with one of them corresponding to 6-phospho-1-fructokinase (PFK). This enzyme catalyses the phosphorylation of fructose 6-phosphate (F6P) to fructose 1,6-bisphosphate, an early step in the glycolytic pathway in *Tc* [39,40]. Considering its crucial biological role, PFK, has been previously identified as a promising and selective therapeutic target for the chemotherapy of diverse diseases caused by several trypanosomatides, including *Tc* [41]. Of note, our metabolic studies in the presence of the inhibitors (section 2.3.2) revealed that they interfered with an early process in the glycolytic cascade, which is consistent with the potential inhibition of PFK. Also, Brimacombeet et al. [42] previously reported a series of PFK inhibitors that are indeed structurally related to the series of NBSBZD reported in this work. The above mentioned aspects, led us to further study the inhibition of FPK elicited by the reported NBSBZD as a pathway for their observed anti-*Tc* activity.

2.4.2. Development of a structure-activity relationship model for the inhibition of PFK

Structurally, PFK exhibits a homotetrameric structure (chains A-D) forming a dimer of dimers. In addition, each monomer chain contains four well defined domains (domains A-D) [39,40], two of which present a compact structure, namely domain B (residues 95–233, 386–409) and domain C (residues 234–385, 442–453), while subdomains A and D present a less organized structure [39,40]. The catalytic site involved in the phosphorylation of fructose 6-phosphate has been characterized in detail [39,40], and includes one subcavity responsible for binding ATP, and a proximal subcavity in which fructose 6-phosphate is bound prior to being phosphorylated. The first one is located in the interface between subdomains B and C of each monomer, while the fructose binding site is formed at the interface between domains B and C, with and additional contribution of a lysine residue (Lys347) belonging to a second protein subunit. Also, it has been reported that significant conformational changes are produced in the apo enzyme (*aTc-PFK*) upon ATP binding [40], leading to a structurally rearranged catalytic site in the holo protein (*hTc-PFK*). Although, the crystallographic structure of *Tc–PFK* has not been solved yet, that of homologous trypanosomatids, such as *Trypanosoma brucei* (Tb-PFK), has indeed been obtained in both the apo and holo forms. A high degree of homology in PFK has been reported in different species, with 77% overall sequence identity and more than 90% sequence identity within the region corresponding the enzyme active site [42,43]. In this way, in the present study, we used available crystallographic structures as templates for homology modeling techniques to obtain three dimensional models of both *aTc-PFK* and *hTc-PFK*. (see Materials and Methods for details).

2.4.2.1. Inhibitor-PFK model development for a training set. A training set of 32 PFK inhibitors reported in the ChEMBL database (Figs. S16–S21) was used to develop a structure-activity relationship model using *aTc-PFK* and *hTc-PFK* as the target enzymes. In this way, molecular docking techniques were used to predict the binding mode to the corresponding catalytic site for each compound in the training set. Docked poses were scored using the ChemGauss3 scoring function as implemented in the FRED docking software [44], with the five lowest energy docked poses being selected for further SAR model development.

Fig. 2 presents the predicted binding mode obtained for the most potent inhibitor within the training set, bound to both the apoenzyme (Fig. 2a) and the holoenzyme (Fig. 2b). In the first case, (*aTc-PFK*), we found that the inhibitor binds to a solvent accessible cleft normally occupied by fructose 6-phosphate during the catalytic cycle, establishing intermolecular interactions with residues Arg173(A), Arg274(A), Glu325(A), Asp339(A), Lys345(A), Leu346(A), Asp348(A), Val351(A), Glu352(A), Tyr375(A), Asp377(A), Tyr380(A) and Lys374(D) (Fig. 2a). Among the key stabilizing interactions, two hydrogen bond contacts with Arg274 and Lys374 anchors the inhibitor to the binding site. When binding to *hTc-PFK* was studied (Fig. 2b), it was found that the inhibitor was positioned within a buried cavity adjacent to the position of the ATP-Mg complex of the holoenzyme, establishing intermolecular contacts with residues Gly198(A), Asp199(A), Gln200(A), Asp231(A), Leu232(A), Arg274(A), Asp275(A), Asn343(A) and Ala430(A) (Fig. 2b). When docking assays were extended to the whole training set, homologous binding modes to those described above were found (depictions not shown).

From the above mentioned aspects, it is clear that the interaction of PFK inhibitors with the target strongly depends on the state of the enzyme (i.e. apo or holo enzyme). To further assess which form of the enzyme may constitute the target of the training set, we searched for a quantitative correlation between the interaction energies of the inhibitors docked to the catalytic sites of *aTc-PFK* and *hTc-PFK* and the reported inhibitory potencies (pIC_{50}). These interaction energies were calculated by applying the MMGBSA method, and considered only the amino acid residues lying within a 5 Å radius from the ligand (Tables S4 and S5). As shown in Fig. 3, the reported inhibitory potencies (pIC_{50}) exhibited a close correlation with the sum of the interaction energies found for *aTc-PFK* (Fig. 3a), while no correlation between the interaction energy and the inhibitory potency was found after docking the training set to *hTc-PFK* (Fig. 3b). These observations strongly suggest that compounds

Table 3
List of *Trypanosoma cruzi* drugabble targets retrieved from the ChEMBL (https://www.ebi.ac.uk/chembl/) database (accession date 2/2018).

Target	UniProt[a]	n[b]
6-phospho-1-fructokinase	Q4E657	42
Bifunctionaldihydrofolatereductase-thymidylate synthase	Q27793	7
Cruzipain	P25779	750
Cyclic nucleotide specific phosphodiesterase	Q53I59	51
Deoxyuridinetriphosphatase	Q4DI50	–
Farnesyldiphosphate synthase	Q8WS26	47
Farnesylsynthetase	Q964Q8	20
Farnesyltransferase	Q4CXF7	–
Glyceraldehyde-3-phosphate dehydrogenase	P22513	39
Hexokinase	Q8ST54	94
Sterol 14-alpha demethylase	Q7Z1V1	–
Trans-sialidase	Q26966	19
Triosephosphateisomerase	P52270	9
Trypanothionereductase	P28593	282

[a] Deposition code in the UniProt database (https://www.uniprot.org/).
[b] Number of chemical entities assayed against the corresponding targets as deposited in ChEMBL.

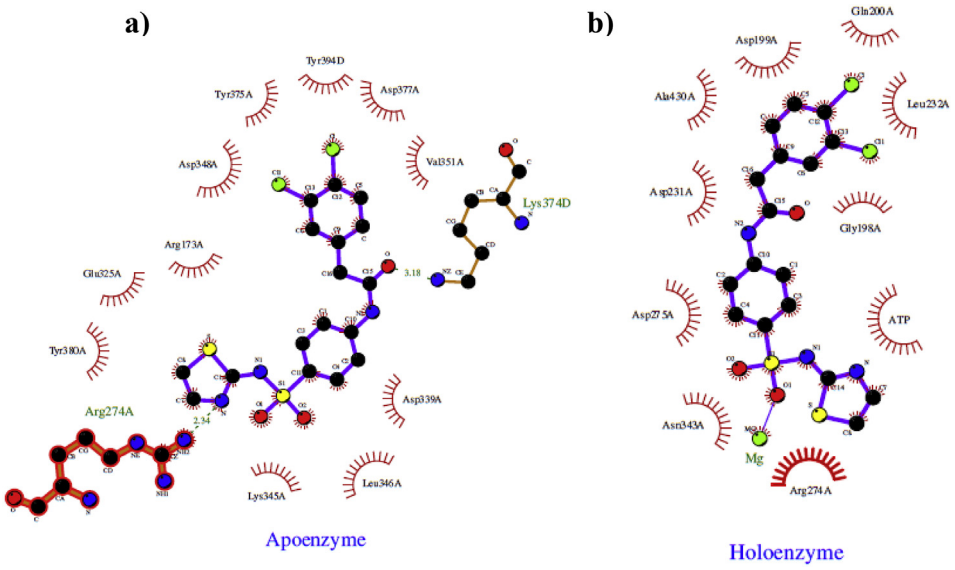

Fig. 2. Intermolecular interactions established by the most active PFK inhibitor belonging to the training set (Fig. S21, TS32) with residues of: a) *a*Tc-PFK and b) *h*Tc-PFK.

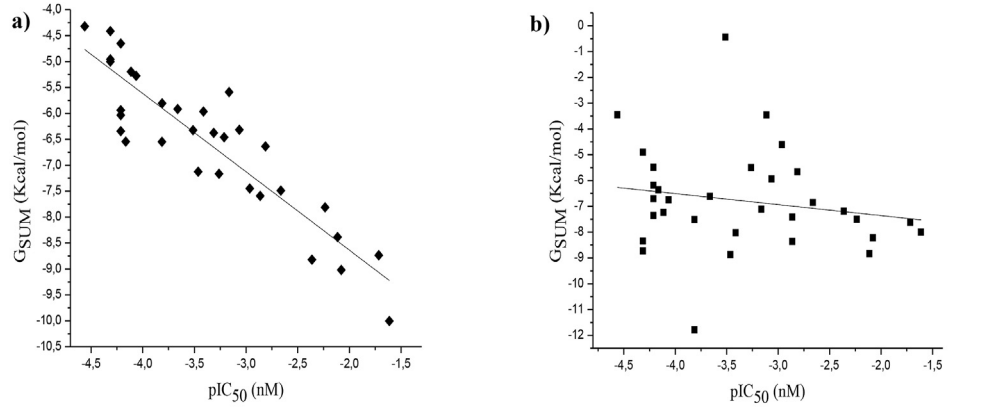

Fig. 3. Correlation between the sum of energetic components (ΔG_{SUM}) determined by molecular docking (Tables S4 and S5) and the reported biological activity (pIC_{50}) for the interaction of the training set with a) *aTc-PFK* and b) *hTc-PFK*.

included in the training set inhibits the enzyme by binding to the PFK catalytic site in the *apo* form.

2.4.3. Modeling of aTc-PFK inhibition elicited by NBSBZD

In order to study if the bioactivity observed for the series of synthesized NBSBZD compounds is elicited by the inhibition of PFK, and particularly through binding to *aTc-PFK*, the set of 14 derivatives was subjected to molecular docking studies and energy calculation protocols described above for the training set. As a general overview of the overall binding mode of the serie of NBSBZD and the previously reported compounds in the training set, Fig. 4 presents a superimposition of the binding mode of the most active inhibitor within the training set (TS32, thinner licorice) and the most active NBSBZD derivative.

As before, the sum of interaction components was calculated within a 5 Å radius from the ligand (Table S6), with the calculated pIC50 values being obtained by applying the equation shown in Fig. 3.a. As can be seen, a good correlation between pIC_{50calc} and pIC_{50exp} was observed (Fig. 5), strongly suggesting that *aTc-PFK* constitutes the molecular target mediating the anti *Tc* activity of the studied set of NBSBZD derivatives.

3. Conclusions

A series of new 14 NBSBZD were synthesized and their structures were characterized. All compounds exhibited adequate drug-like properties, with Lipinski parameters showing that they may exhibit good membrane permeability and adequate oral bioavailability. Also, screening of the synthesized compounds through the OSIRIS database resulted in lower tumorigenic risk or irritant and reproductive side-effects than the reported NBSBZD compared to the reference compounds BZN and NFX.

In vitro assays were conducted in order to evaluate the anti-trypanosomal activity and toxicity towards Vero cells. Compounds **2**, **9** and **14** displayed the highest inhibitory potencies against the epimastigote and amastigote forms of *Tc*, with a marked increase in their bioactivities compared to the reference compound BZN. In addition, a significant increase in the SI was calculated for all the reported compounds.

In order to study the mechanism of the anti-*Tc* activity of the

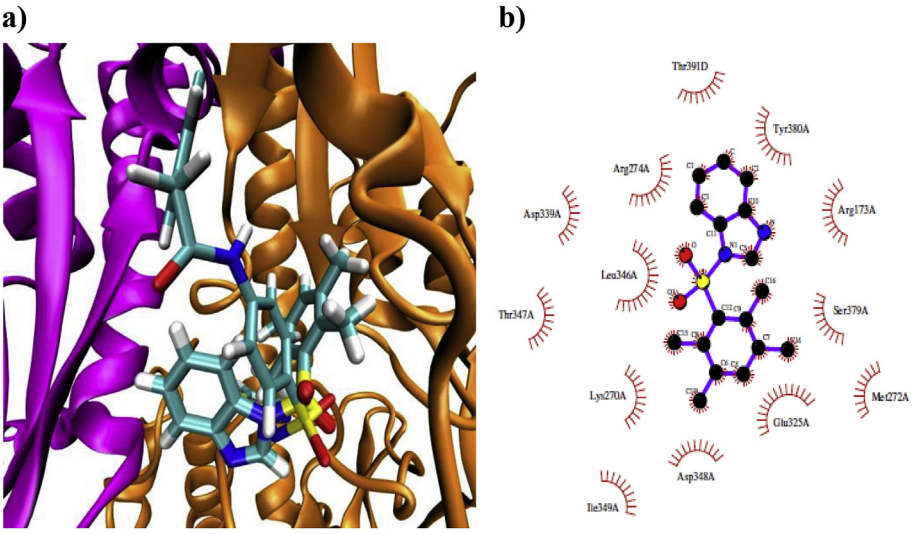

Fig. 4. Superimposition of the binding modes of the most active inhibitor within the training set (TS32, thinner licorice) and the most active NBSBZD derivative (Fig. 1, Cpd. 14, wider licorice) to a) *aTc-PFK* and b) *hTc-PFK*.

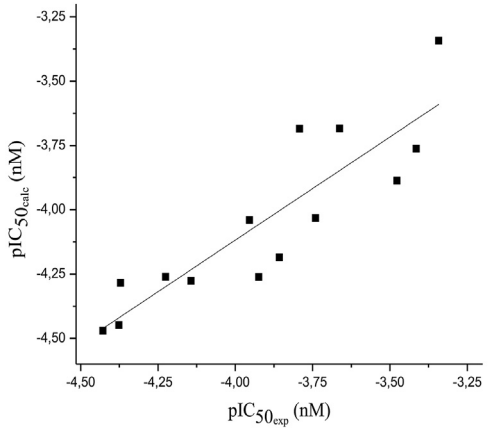

$\mathbf{pIC_{50calc}} = 0.802\ (\pm 0.125)\ \mathbf{pIC_{50exp}} - 0.910\ (\pm 0.489)$

$r = 0.881,\ r^2 = 0.775,\ sd = 0.163,\ F = 41.411,\ n = 14$

Fig. 5. Correlation between the experimental biological activity (pIC_{50exp}) and the corresponding activity predicted based on the developed QSAR model for Cpds 1–14 (pIC_{50calc}).

reported molecules, a combination of metabolite excretion studies and molecular modeling techniques was used. Both, the experimental and theoretical approaches were consistent in that the target of the assayed compounds is related to the glycolytic pathway of the parasite. Specifically, molecular modeling studies strongly supported the binding of the studied compounds to the apo form of PFK as the molecular target of the observed biological activity.

From the presented results, we can conclude that the series of NBSBZD synthesized constitutes a significant potential as anti *Tc* agents, representing a valuable contribution towards the further design of antichagasic compounds based on the NBSBZD scaffold.

4. Experimental section

4.1. General considerations

Melting points (mp) were determined by using an electrothermal apparatus, by microcapillary methods and are uncorrected. Infrared spectra were recorded on a Nicolet 5 SXC FT-IR. NMR experiments were performed on a Bruker Advance II 400 Hz, ultrashield TM spectrometer at 400.16(^{1}H) and 100.62 (^{13}C) equipped with an inverse multinuclear detection probe, digital resolution capabilities and a variable temperature unit. Chemical shift values are reported in ppm, while the multiplicities of the signals are described using the following abbreviations s = singlet, d = doublet, t = triplet, q = quartet, sex = sextet, m = multiplet, and were acquired in $CHCl_3$-d as solvent (referred to residual $CHCl_3$ at 7.26 ppm for ^{1}H and 77 ppm for ^{13}C). Coupling constants (*J*) are in Hz. High resolution mass spectroscopy experiments were acquired using a Micromass Q-TOF micro hybrid quadrupole/orthogonal high resolution time of flight MS equipped with a Micromass capillary HPLC (Waters Corporation). The benzimidazole and all the arylsulfonyl chlorides were purchased from Sigma-Aldrich and Acros Organics. Pyridine used for synthetic procedures was distilled prior to use and stored over pellets of NaOH. All other reagents and solvents (p.a. grade) were used as purchased from Dorwill, Biopack, Sintorgan and Merck.

4.2. General synthetic procedure

A mixture of the benzimidazole (3 mmol), 1.5 mL of anhydrous pyridine and methylene chloride (15 mL) was stirred at room temperature for 1 h, after which the corresponding arylsulfonyl chloride (3.2 mmol) was added. The mixture was stirred for 1 h and the completion of the reaction was tested by TLC using hexane:acetone (7:3) or chloroform:methanol:acetone (8:1:1) as the mobile phase. The sulfonylation time was around 1 h, after which the reaction was stopped by the addition of HCl 10% (30 mL). The resulting immiscible phases were separated, with the organic phase being extracted by sequentially adding HCl 10% (1 × 30 mL), a saturated Na_2CO_3 solution (1 × 30 mL) and brine (1 × 30 mL). The resulting organic phase was dried over anhydrous $MgSO_4$, filtered and concentrated to dryness under vacuum to isolate the reaction products as solids. End-products were purified by crystallisation from ethanol, n-hexane or mixtures of them.

4.2.1. Specific procedures and spectral data for compounds 1–7, 9, 11–16

- 1-(Benzenesulfonyl)-benzimidazole**(1).** [26] White crystals (0.55 g, 79%). mp. 99–100 °C (from *n*-hexane). **IR** (νmax/cm^{-1}, KBr):

3066 (νCH), 1376 (νSO_{2asim}), 1171 (νSO_{2sim}). **^{1}HNMR** ($CDCl_3$, 400.16 Hz): 8.39 (s,1H,H2); 8.00 (d, 2H, 8.6 Hz, H2'); 7.87 (d, 1H, 7.76 Hz, H8); 7.77 (d, 1H, 8.6 Hz, H5); 7.64 (t, 1H, 6.88 Hz, H4'); 7.53 (t, 1H, 8.64 Hz, H3'); 7.39 (m, 2H, H6–H7).**^{13}CNMR** ($CDCl_3$, 100.62 Hz; assigned using HSQC): 144.23 (Cq-4); 141.22 (CH-2); 137.70 (Cq-1'); 134.95 (CH-4'); 130.94 (Cq-9); 129.83 (CH-3'); 127.42 (CH-2'); 125.65 (CH-6); 124.84 (CH-7); 121.40 (CH-8); 112.63 (CH-5). **HRMS (EI)** *m/z*: calculated mass for C13H10N2O2S1: 258.1000, found: 259.0000 $[M+H]^+$ [26].

- 1-(4-Acetamide-benzenesulfonyl)-benzimidazole (**2**). White crystals (0.58 g, 76%). mp. 186 °C - decomposition (from EtOH). **IR**(νmax/cm^{-1}, KBr): 3244 (νNH), 3037 (νCH), 1701 (νCO), 1377 (νSO_{2asim}), 1162 (νSO_{2sim}). **^{1}HNMR** ($CDCl_3$, 400.16 Hz): 8.37 (s, 1H, H2); 7.94 (dd, 2H,8 Hz, H2'); 7.85 (d, 1H, 6.6 Hz, H8); 7.76 (d, 1H, 6.56 Hz, H5); 7.67 (d, 2H, 8.2 Hz, H3'); 7.40 (sa, 1H, H10); 7.38 (m, 2H, H6 and H7); 2.05 (s, H,H12). **^{13}CNMR** ($CDCl_3$, 100.62 Hz; assigned using HSQC): 168.44 (C6' = O); 144.0 (Cq-9); 143.70 (Cq-4'); 141.17 (Cq-2); 131.83 (Cq-1'); 130.72 (Cq-4); 128.78 (CH-2'); 125.63 (CH-7); 124.84 (CH-6); 121.09 (CH-8); 119.48 (CH-3'); 112.47 (CH-5); 24.74 (CH_3-7'). **HRMS (EI)** *m/z*: calculated mass for C15H13N3O3S1: 338.0570, found: 338.0653 [M+Na].

- 1-(4-acetyl-benzenesulfonyl)-benzimidazole (**3**). White crystals (0.31 g, 92%). mp. 119–120 °C (from EtOH→*n*-hexane). **IR**(ν max/cm^{-1}, KBr): 3039 (νCH), 2967 (νCH_3), 1684 (νC = O), 1381 (νSO_{2asim}), 1163 (νSO_{2sim}). **^{1}H NMR** ($CDCl_3$, 400.16 Hz): 8.39 (s, 1H, H2); 8.07 (quadruplet, 4H, 8.4 Hz, H3'-H2'); 7.87 (d, 1H, 7.68 Hz, H8); 7.78 (d, 1H, 6.6 Hz, H5); 7.40 (m, 2H, H6–H7), 2.60 (s, 3H, H6'). **^{13}C NMR** ($CDCl_3$, 100.62 Hz; assigned using HSQC): 196.00 (C═O), 144.07 (Cq-9); 141.55 (Cq-1'); 141.05 (CH-2); 130.64 (Cq-4); 129.40 (CH-2'); 127.54 (CH-3'); 125.93 (CH-6); 125.18 (CH-7); 121.34 (CH-8); 112.39 (CH-5); 26.82 (CH3-6'). **HRMS (EI)** *m/z*: calculated mass for C15H12N2O3S1: 301.0641, found: 301.0644 [M+H]+, calculated mass for C15H12N2O3S1Na: 323.0461, found: 323.0466 [M+Na].

- 1-(4-Methyl-benzenesulfonyl)-benzimidazole (**4**) [27]. White crystals (0.5 g, 86%). mp. 74–75 °C (from EtOH/n-hexane). **IR**(νmax/ cm^{-1}, KBr): 3054 (νCH), 2963, 2869 (νCH_3), 1378 (νSO_{2asim}), 1169 (νSO_{2sim}). **^{1}HNMR** ($CDCl_3$, 400.16 Hz): 8.38 (s, 1H, H2); 7.87 (m, 3H, H2'-H8); 7.76 (d, 1H, 5.5 Hz, H5); 7.37 (m, 2H, H6–H7); 7.31 (d, 2H, H3'). **^{13}CNMR** ($CDCl_3$, 100.62 Hz; assigned using HSQC): 146.18 (Cq-4'); 144.07 (Cq-9); 141.24 (CH-2); 134.64 (CH-1); 130.80 (CH-4); 127.37 (CH-2'); 125.54 (CH-6); 124.75 (CH-7); 121.08 (CH-8); 112.5 (CH-5); 21.65 (CH_3-5'). MS *m/z*: mass found for C14H12N2O2S1: 272.00 $[M]^+$ [27].

-1-(4-Fluoro-benzenesulfonyl)-benzimidazole (**5**). White crystals (0.53 g, 64%). mp. 124–125 °C (from EtOH→*n*-hexane). **IR**(ν max/cm^{-1}, KBr): 3071 (νCH), 1377 (νSO_{2asim}), 1159 (νSO_{2sim}), 1086 νCF. **^{1}HNMR** ($CDCl_3$, 400.16 Hz): 8.37 (s, 1H, H2); 8.03 (ddd, 2H, 7 and 2 Hz, $JHF_{(orto)} = 4.9$, H2'); 7.85 (d, 1H, 6.76 and 1.36 Hz, H8); 7.78 (d, 1H, 7.16 and 1.88 Hz, H5); 7.40 (m, 2H, H6–H7); 7.20 (td, 2H, 8.72 and 2 Hz, H3'). **^{13}CNMR** ($CDCl_3$, 100.62 Hz; assigned using HSQC): 166.28 (Cq-4', $^1JCF = 260$ Hz); 144.06 (Cq-9); 141.08 (CH-2); 133.38 (Cq-1'); 130.63 (Cq-4); 130.21 (CH-2'); 125.82 (CH-7); 125.05 (CH-6); 121.28 (CH-8); 117.26 (CH-3'); 112.36 (CH-5). **HRMS (EI)** *m/z*: calculated mass for C13H9F1N2O2S1Na: 299.0261, found: 299.0272 [M+Na].

- 1-(4-Chloro-benzenesulfonyl)-benzimidazole (**6**). [27] White crystals (0.62 g, 63%). mp. 113–114 °C (from EtOH). **IR** (νmax/cm^{-1}, KBr): 3058 (νCH), 1384 (νSO_{2asim}), 1171 (νSO_{2sim}), 761 (νCCl). **^{1}HNMR** ($CDCl_3$, 400.16 Hz): 8.37 (s, 1H, H2); 7.93 (dd, 2H, 9.3 and 1.3 Hz, H2'); 7.84 (d, 1H, 7.96 and 1.36 Hz, H8); 7.78 (d, 1H, 7.92 and 1.36 Hz, H5); 7.50 (dd, 2H, 9.3 and 1.3 Hz, H3'); 7.4 (m, 2H, H6–H7).**^{13}CNMR** ($CDCl_3$, 100.62 Hz; assigned using HSQC): 144.04 (Cq-9); 141.81 (Cq-4'); 141.1 (CH-2); 135.93 (CH-1); 130.6 (Cq-4); 130.15 (CH-2'); 128.6 (CH-3'); 125.85 (CH-7); 125.1 (CH-6); 121.3 (CH-8); 122.36 (CH-5). **HRMS (EI)** *m/z*: calculated mass for C13H9Cl1N2O2S1Na: 314.9965, found: 314.9970 [M+Na].

- 1-(4-Bromo-benzenesulfonyl)-benzimidazole (**7**). White crystals(0.57 g, 54%). mp. 129–130 °C (from EtOH). **IR**(νmax/cm^{-1}, KBr): 3086 (νCH), 1381 (νSO_{2asim}), 1163 (νSO_{2sim}), 746 (νCBr). **^{1}HNMR** ($CDCl_3$, 400.16 Hz): 8.36 (s, 1H, H2); 7.85 (m, 3H, H3'-H8); 7.78 (d, 1H, 7 and 0.8 Hz, H5); 7.66 (dd, 2H, 8.9 and 2 Hz, H2'); 7.4 (m, 2H, H6–H7). **^{13}CNMR** ($CDCl_3$, 100.62 Hz; assigned using HSQC): 144.07 (Cq-9); 141.03 (CH-2); 136.5 (Cq-4'); 133.05 (CH-2'); 131.1 (Cq-4); 130.4 (Cq-1'); 128.6 (CH-3'); 125.95 (CH-7); 125.2 (CH-6); 121.32 (CH-8); 122.25 (CH-5). **HRMS (EI)** *m/z*: calculated mass for C13H9Br1N2O2S1Na: 358.9460, found: 358.9464 [M+Na].

- 1-(2-Nitro-benzenesulfonyl)-benzimidazole (**8**). Yellow crystals (0.36 g, 72%). mp. 117–118 °C (from EtOH). **IR** (νmax/cm^{-1}, KBr): 3022 (νCH), 1527 (νNO_{2asim}), 1388 (νSO_{2asim}), 1352 (νNO_{2sim}), 1152 (νSO_{2sim}). **^{1}H NMR** ($CDCl_3$, 400.16 Hz): 8.5 (s, 1H,H2); 8.30 (m, 1H, 9.5 y 3.3 Hz, H3'a); 7.8 (m, 3H,H4'-H2'b-H3'b); 7.7 (m, 2H, H5–H8); 7.42 (m, 2H, H7–H6). **^{13}CNMR** ($CDCl_3$, 100.62 Hz; assigned using HSQC): 148.1 (Cq-2'a); 143.9 (Cq-9); 142.2 (CH-2); 136.0 (CH-3'b); 134.5 (Cq-4); 132.7 (CH-4'); 131.3 (CH-3'a); 130.46 (Cq-1'); 126.5 (CH-7); 125.7 (CH-6); 125.0 (CH-2'b); 121.5 (CH-8); 112.2 (CH-5). **HRMS (EI)** *m/z*: calculated mass for C13H9N3O4S1: 304.0387, found: 304.0390 $[M+H]^+$, calculated mass for C13H9N3O4S1Na: 326.0206, found: 326.0208 [M+Na].

- 1-(3-Nitro-benzenesulfonyl)-benzimidazole (**9**). Yellow crystals (0.63 g, 64%). mp. 151–152 °C (from EtOH). **IR** (νmax/cm^{-1}, KBr): 3022 (νCH), 1527 (νNO_{2asim}), 1388 (νSO_{2asim}), 1352 (νNO_{2sim}), 1152 (νSO_{2sim}).**^{1}HNMR** ($CDCl_3$, 400.16 Hz): 8.9 (t, 1H,H2'a); 8.50 (ddd, 1H, 7.24, 2 and 1 Hz, H4'); 8.4 (s, 1H,H2); 8.3 (ddd, 1H, 6.93, 1.8 and 1 Hz, H2'b); 7.92 (d,1H, 7.44 and 0.72 Hz, H8); 7.8 (m, 2H, H5–H3'b); 7.48 (td, 1H, 7.48 and 1.2 Hz, H7); 7.48 (td, 1H, 7.44 y 1.2 Hz,H6). **^{13}CNMR** ($CDCl_3$, 100.62 Hz; assigned using HSQC): 148.5 (Cq-3'a); 144.1 (Cq-9); 140.84 (CH-2); 139.6 (Cq-1'); 132.36 (CH-2'b); 131.35 (CH-3'b); 130.46 (Cq-4); 129.17 (CH-4'); 126.28 (CH-7); 125.49 (CH-6); 122.52 (CH-2'a); 121.55 (CH-8); 112.26 (CH-5). **HRMS (EI)** *m/z*: calculated mass for C13H9N3O4S1: 304.0387, found: 304,0390 $[M+H]^+$, calculated mass for C13H9N3O4S1Na: 326.0206, found: 326.0208 [M+Na].

- 1-(4-Nitro-benzenesulfonyl)-benzimidazole (**10**). Yellow crystals (0.73 g, 73%). mp. 153–154 °C (from EtOH). **IR**(νmax/cm^{-1}, KBr): 3026 (νCH), 1533 (νNO_{2asim}), 1388 (νSO_{2asim}), 1351 (νNO_{2sim}), 1172 (νSO_{2sim}). **^{1}HNMR** ($CDCl_3$, 400.16 Hz): 8.36 (m, 2H, H3'-H2); 8.2 (dd, 2H, 9.3 and 2.4 Hz, H2'); 7.85 (d, 1H, 8 and 1.3 Hz, H8); 7.78 (d, 1H, 7.9 and 1.3 Hz, H5); 7.4 (m, 2H, H6–H7). **^{13}CNMR** ($CDCl_3$, 100.62 Hz; assigned using HSQC): 151.3 (Cq-4'); 144.3 (Cq-9); 143.22 (Cq-1'); 140.97 (CH-2); 130.6 (Cq-4); 128.5 (CH-2'); 126.6 (CH-7); 125.75 (CH-6); 124.9 (CH-3'); 121.7 (CH-8); 112.19 (CH-5). **HRMS (EI)** *m/z*: calculated mass for C13H9N3O4S1Na: 326.0206, found: 326.0206 [M+Na].

- 1-(3-trifluoromethyl-benzenesulfonyl)-benzimidazole (**11**). White crystals (0.44 g, 87%). mp. 83–84 °C (from EtOH). **IR**(νmax/ cm^{-1}, KBr): 3025 (νCH), 1332 (νSO_{2asim}), 1165 (νSO_{2sim}), 1133 (νCF_{3asim}), 1099 νCF. **^{1}H NMR**($CDCl_3$, 400.16 Hz): 8.39 (s, 1H, H2); 8.28 (s, 1H, H2'a); 8.17 (d, 1H, 8.32 Hz, H2'b); 7.87 (m, 2H, H4'-H8); 7.79 (d, 1H, 7.0 Hz, H5); 7.70 (t,1H, 5.32 Hz, H3'b); 7.44 (t, 1H, 7.04 Hz, H7), 7.39 (t, 1H, 7.04 Hz, H6). **^{13}CNMR** ($CDCl_3$, 100.62 Hz; assigned using HSQC): 144.09 (Cq-9); 140.96 (CH-2); 138.85 (Cq-1'); 131.45 (CH-4', $^3JCF = 3.35$ Hz); 130.7 (CH-3'b); 130.58 (Cq-4); 130.26 (CH-2'b-Cq-3'a $^2JCF = 40.2$ Hz); 126.13 (CH-7); 125.26 (CH-6); 124.28 (CH-2'a $^3JCF = 3.86$ Hz- Cq-5'); 121.49 (CH-8); 112.20 (CH-5); 30.59 (Cq-6'). **HRMS (EI)** *m/z*: calculated mass for C14H9F3N2O2S1: 327.0410, found: 327.0415 $[M+H]^+$.

- 1-(4-trifluoromethyl-benzenesulfonyl)-benzimidazole (**12**). White crystals(0.51 g, 83%). mp. 99–100 °C (from EtOH). **IR**(νmax/ cm^{-1}, KBr): 3046 (νCH), 1321 ($\nu SO_{2\ asim}$), 1175 (νSO_{2sim}), 1135 (νCF_{3asim}), 1090 νCF. **^{1}H NMR**($CDCl_3$, 400.16 Hz): 8.39 (s, 1H, H2);

8.14 (d, 2H, 7.5 Hz, H2'); 7.87 (d, 1H, 9.8 y 3.44 Hz, H8); 7.81 (d, 3H, H3'-H5); 7.41 (m, 2H, H7–H6). **^{13}C NMR** ($CDCl_3$, 100.62 Hz; assigned using HSQC): 144.62 (Cq-9); 141.09 (CH-2); 136.25 (Cq-4', ^{2}JCF = 33.20 Hz); 130.96 (Cq-4); 128.1 (Cq-1',CH-2'); 126.56 (CH-3', Cq-5', ^{3}JCF = 4.0 Hz); 126.07 (CH-7); 125.46 (CH-6); 121.5 (CH-8); 112.48 (CH-5). **HRMS (EI)** *m/z*: calculated mass for C14H9F3N2O2S1: 327.0410, found: 327.0422 $[M+H]^+$.

- 1-(4-*t*-butyl-benzenesulfonyl)-benzimidazole (**13**). [27] White crystals (0.5 g,80%). mp. 116–117 °C (from EtOH→*n*-hexane). **IR** (νmax/cm^{-1}, KBr): 3054 (νCH), 2963, 2869 (νCH_3), 1378 (νSO_{2asim}), 1169 (νSO_{2sim}). **^{1}HNMR**($CDCl_3$, 400.16 Hz): 8.39 (s, 1H, H2); 7.92 (m, 3H, H2'-H8); 7.78 (d, 1H, 7.2 and 0.72 Hz, H5); 7.52 (dd, 2H, H3'); 7.41 (t, 1H, 7.3 and 1 Hz, H7); 7.37 (t, 1H, 7.76 and 1.64 Hz, H6); 1.28 (s, 9H, H6'). **^{13}C NMR** ($CDCl_3$, 100,62 Hz; assigned using HSQC): 159.26 (Cq-4'); 144.28 (Cq-9); 141.34 (CH-2); 134.7 (CH-1); 130.84 (CH-4); 127.44 (CH-2'); 126.51 (CH-3'); 125.28 (CH-7); 124.7 (CH-6); 121.61 (CH-8); 112.61 (CH-5); 35.53 (Cq-5'); 30.59 (CH3-6'). **MS** *m/z*: found C17H19N2O2S1:314.00 $[M]^+$ [27].

- 1-(2, 3, 5, 6-tetramethyl-benzenesulfonyl)-benzimidazole (**14**). White crystals(0.49 g, 82%). mp. 130–131 °C (from EtOH). **IR** (νmax/cm^{-1}, KBr): 3089 (νCH), 2973,2918(νCH_3), 1603 (aromatic substitution 1,2,3,5,6), 1463,1432 (δCH_3), 1357 (νSO_{2asim}), 1158 (νSO_{2sim}). **^{1}H NMR** ($CDCl_3$, 400.16 Hz): 8.40 (s, 1H, H2); 7.78 (d, 1H, 7.96 and 0.8 Hz, H8); 7.32 (td, 1H, 7.28 and 1.2 Hz, H7); 7.24 (m, 2H, H4'-H6); 7.16 (d, 1H, 7.44 y 0.7 Hz, H5); 2.47 (s, 6H, H6'); 2.23 (s, 6H, H5'). **^{13}C NMR**($CDCl_3$, 100.62 Hz; assigned using HSQC): 143.63 (Cq-9); 141.3 (CH-2); 137.84 (Cq-1'-4'); 136.8 (CH-3'); 136.34 (CH-2'); 131.07 (Cq-4); 125.02 (CH-6); 124.37 (CH-7); 120.9 (CH-8); 111.9 (CH-5), 21.0 (CH3-6'),17,5 (CH3-5'). **HRMS (EI)** *m/z*: calculated mass for C17H18N2O2S1Na: 337.0981, found: 337.0994 [M+Na].

4.3. Biological evaluation

4.3.1. Parasite strain culture

Epimastigotes of *Tc* SN3 strain (IRHOD/CO/2008/SN3) isolated from domestic *Rhodnius prolixus* from Guajira (Colombia) [33], were cultured *in vitro* in trypanosomes liquid medium (TLM) with 10% inactivated foetal bovine serum, and were kept in an air atmosphere at 28 °C in Roux flasks (Corning, USA) with a surface area of 75 cm^2, according to a previously described methodology [34].

4.3.2. Cell culture and cytotoxicity tests

Vero cells (EACC number 84113001) originally obtained from monkey kidney were grown in RPMI medium (Gibco), supplemented with 10% inactivated of foetal bovine serum in a humidified 95% air, 5% CO2 atmosphere at 37 °C for two days. The cytotoxicity test for Vero cells was performed according to a previously described methodology [34]. After 72 h of treatment, cell viability was determined by flow cytometry. Thus, 100 mL/well of a propidium iodide solution (100 mg/mL) was added and incubated for 10 min at 28 °C in darkness. Afterwards, 100 mL/well of fluorescein diacetate (100 ng/mL) was added and incubated under the same conditions. Finally, the cells were recovered by centrifugation at 400*g* for 10 min, with the pellet being washed with phosphate buffered saline (PBS). Flow cytometry analysis was performed with a FACS Vantage flow cytometer (Becton Dickinson). The percentage of viability was calculated by comparison with the corresponding control cultures. The IC_{50} was calculated using the software PROBIT.

4.3.3. In vitro activity: epimastigote assay (extracellular forms)

The assay was performed following a previously reported procedure [34]. Briefly, assayed compounds and the reference drug benznidazole (BZN) were dissolved in a PEG:EtOH mixture (7:3), which was been previously found to be non-toxic and lacking any inhibitory effects on parasite growth. Compounds were added to the culture medium to reach final concentrations of 1, 10, 25 and 50 μM, measuring the effect of each compound against *Tc* epimastigotes during 72 h using a Neubauer haemocytometer. The anti-Chagas effect is expressed as the IC_{50}, which was calculated using the PROBIT software and corresponded to the concentration required to produce 50% growth inhibition. The corresponding results are expressed as the average of three separate experiments.

4.3.4. In vitro activity: amastigotes assay (intracellular forms)

Vero cells were grown in RPMI medium (Gibco) supplemented with 10% inactivated foetal bovine serum and were kept in a humidified atmosphere of 95% air and 5% CO2 at 37 °C. Cells were seeded at a density of 1×10^4 cells/well in 24-well microplates (Nunc) with rounded cover slips on the bottom and cultured for 2 days. Afterwards the cells were infected *in vitro* with metacyclic forms of *Tc* at a ratio of 10:1 during 24 h [35]. The non-phagocytosed parasites were removed by washing, and then the assayed compounds were added to reach final concentrations of 1, 10, 25 and 50 μM. The resulting Vero cells were incubated for 72 h at 37 °C in a 5% CO2 atmosphere. Drug activity was determined on the basis of number of amastigotes in treated and untreated cultures in methanol-fixed and Giemsa-stained preparations. The number of amastigotes was determined by analyzing 200 host cells distributed in randomly chosen microscopic fields. The anti-Chagas effect is expressed as the IC_{50}. The results presented in Table 1 are averages of three separate experiments.

4.3.5. Metabolites excretion study

Cultures of *Tc* epimastigotes (initial concentration of 5×10^5 cells/mL) received IC_{25} concentrations of the compounds under study (except for control cultures). After incubation during 96 h at 28 °C, the cells were centrifuged at 400 g for 10 min. The supernatants were collected to determine the excreted metabolites using ^{1}H NMR. Chemical shifts were expressed in parts per million (ppm, δ scale), using sodium 2,2-dimethyl-2-silapentane-5-sulfonate as the reference signal. The chemical displacements used to identify the respective metabolites were consistent with those previously described [30].

4.4. Molecular modeling studies

4.4.1. Development of Tc–PFK homology models

The homology modeling of *Tc*PFK was based on the crystallographic structure of *Tb*PFK [39,40]. The three-dimensional structure was constructed using Modeller v9.16 software [45], with the sequence corresponding to *Tc*PFK being downloaded from the UniProt database [38]. Then both PFK sequences were aligned and compared, reaching 76.7% sequence identities, in agreement with previous reports [42,43].

Considering that the target can adopt two different conformations, and that the corresponding binding site for the training set under study was unknown, two 3D *Tc*PFK homology models were generated using different crystallographic structures from *Tb*PFK as 3D templates: 1) the apoenzyme form (PDB code: 2HIG) [39] and 2) the holoenzyme form containing the ATP-Mg complex bound to the active site (PDB code: 3F5M) [40]. In order to model the entire active site, the homology model was constructed based on chain A and B. Five 3D homology models were generated for every form of the PFK, with the best model being chosen on the basis of their discrete optimised protein energy (DOPE) score as calculated by Modeller v9.16. The model exhibiting the lowest DOPE value was used for further analysis.

The resulting *aTcPFK* and *hTcPFK* structures were further refined using molecular dynamics simulations. The Amber16 software package was used [46], applying molecular mechanics parameters

corresponding to the Amber *ff14SB* force field [47]. The parameterised systems were submitted to a standard minimisation protocol, applying 5000 steps of computation (2500 steps of steepest descent and 25000 conjugate gradient searches). The resulting structures were used as structural templates for molecular docking studies.

4.4.2. Molecular docking procedures

In order to elucidate the molecular target responsible of the anti-*Tc* activity of the NBSBZD, molecular docking studies were initiated against diverse known targets of *Tc*. Among them, cruzipain was initially screened using the AutoDock software; however a lack of correlation between the corresponding binding modes and the observed anti-*Tc* activity was found.

In a next stage, PFK was screened as potential target involved in the anti-*Tc* activity. In this case, docking procedures were performed using software packages developed by OpenEye Scientific Software [48], and consisted of three sequential stages: 1) the ligand conformer library generation stage, which was conducted using an energy threshold of 10 kcal/mol using the OMEGA software, [49,50]. Stage 2), the docking runs, were performed using the fast rigid exhaustive docking approach implemented in the FRED3 software [44,51,52]. In this case, the ChemGauss3 scoring function was used to evaluate and score resulting docked poses. The five lowest energy docked poses were selected for model development. Stage 3 involved a three-dimensional visualisation and intermolecular interaction analyses, which were performed using the VIDA and LigPlot + software packages [53,54], respectively.

4.4.3. Calculation of intermolecular interaction energies

In order to calculate the interaction energy between the studied ligands and the corresponding protein targets, the free energy of binding was calculated using the molecular mechanics/Poisson-Boltzmann surface area method implemented in MMPBSA. py [55], which is part of the Amber16 distribution [46]. The energy of binding was estimated by taking into account the solvation energies of the interacting molecules, in addition to the molecular mechanics (MM) energies. The contribution of polar solvation energies was computed by generalised Born (GB) implicit solvent model, while the non-polar contribution of the solvation energy was dependent on the solvent accessible surface area (SA) [56]. The corresponding intermolecular complexes were obtained from the molecular docking procedures and subjected to a per-residue free energy binding decomposition analyses. The interaction hotspots were identified taking as reference a 5 Å radius around the docked position of the most active ligand present in the training set. The sum of interaction energies with the corresponding hotspots was afterwards correlated with the biological activity values reported for the ligands included in the training set.

Acknowledgements

This work was supported by SECyT-UNC and MinCyT-Cba (Argentina). G.E.M. acknowledges the CONICET scholarship, and AUIP for supporting an international exchange to UGR (Spain). The authors would also like to thank CCAD at Universidad Nacional de Córdoba (http://ccad.unc.edu.ar/) and the GPGPU Computing Group from the Facultad de Matemática, Astronomía y Física (FAMAF), Universidad Nacional de Córdoba, Argentina, for providing access to computing resources. Mario A. Quevedo wishes to thank OpenEye Scientific Software and their Free Academic Licensing for providing licenses to use the corresponding software packages. Finally, Mario A. Quevedo and Sergio Ribone gratefully acknowledge the support of the NVIDIA Corporation with the donation of the Titan Xp GPU used for this research in the context of the NVIDIA GPU Grant Program.

Appendix A. Supplementary data

Supplementary data to this article can be found online at https://doi.org/10.1016/j.ejmech.2019.01.013.

References

[1] World Health Organization, Investing to overcome the global impact of neglected tropical diseases: third WHO report on neglected tropical diseases 2015, vol. 3, 2015.
[2] J.A. Pérez-Molina, I. Molina, Chagas disease, Lancet (2017) 391. https://doi.org/10.1016/S0140-6736(17)31612-4.
[3] R. Viotti, C. Vigliano, B. Lococo, M.G. Alvarez, M. Petti, G. Bertocchi, A. Armenti, Side effects of benznidazole as treatment in chronic Chagas disease: fears and realities, Expert Rev. Anti Infect. Ther. 7 (2009) 157–163. https://doi.org/10.1586/14787210.7.2.157.
[4] J. Castro, E. de Toranzo Diaz, Toxic effects of nifurtimox and benznidazole, two drugs used against American trypanosomiasis (Chagas' disease), Biomed. Environ. Sci. 1 (1988) 19–33.
[5] J.A. Castro, M.M. deMecca, L.C. Bartel, Toxic side effects of drugs used to treat Chagas' disease (American trypanosomiasis), Hum. Exp. Toxicol. 25 (2006) 471–479. https://doi.org/10.1191/0960327106het653oa.
[6] S.R. Wilkinson, J.M. Kelly, Trypanocidal drugs: mechanisms, resistance and new targets, Expert Rev. Mol. Med. 11 (2009). https://doi.org/10.1017/S1462399409001252.
[7] R.J. Pagliero, S. Lusvarghi, A.B. Pierini, R. Brun, M.R. Mazzieri, Synthesis, stereoelectronic characterization and antiparasitic activity of new 1-benzenesulfonyl-2-methyl-1, 2, 3, 4-tetrahydroquinolines, Bioorg. Med. Chem. 18 (2010) 142–150. https://doi.org/10.1016/j.bmc.2009.11.010.
[8] R. Pagliero, A. Pierini, R. Brun, M. Mazzieri, Design, synthesis and 3-D characterization of 1-benzenesulfonyl-1, 2, 3, 4-tetrahydroquinolines as lead scaffold for antiparasitic drug, Lett. Drug Des. Discov. 7 (2010) 461–470. https://doi.org/10.2174/157018010791306614.
[9] M.C. Becerra, N. Guiñazú, L.Y. Hergert, A. Pellegrini, M. Mazzieri, S. Gea, I. Albesa, In vitro activity of N-benzenesulfonylbenzotriazole on Trypanosoma cruzi epimastigote and trypomastigote forms, Exp. Parasitol. 131 (2012) 57–62. https://doi.org/10.1016/j.exppara.2012.02.028.
[10] R.J. Pagliero, M. Kaiser, R. Brun, M.J. Nieto, M.R. Mazzieri, Lead selection of antiparasitic compounds from a focused library of benzenesulfonyl derivatives of heterocycles, Bioorg. Med. Chem. Lett 27 (2017) 3945–3949. https://doi.org/10.1016/j.bmcl.2017.07.081.
[11] D.A. Erlanson, Fragment-based lead discovery: a chemical update, Curr. Opin. Biotechnol. 17 (2006) 643–652. https://doi.org/10.1016/j.copbio.2006.10.007.
[12] G. Yadav, S. Ganguly, Structure activity relationship (SAR) study of benzimidazole scaffold for different biological activities: A mini-review, Eur. J. Med. Chem. 97 (2015) 419–443. https://doi.org/10.1016/j.ejmech.2014.11.053.
[13] Y. Bansal, O. Silakari, The therapeutic journey of benzimidazoles: a review, Bioorg. Med. Chem. 20 (2012) 6208–6236. https://doi.org/10.1016/j.bmc.2012.09.013.
[14] M. Gaba, S. Singh, C. Mohan, Benzimidazole: an emerging scaffold for analgesic and anti-inflammatory agents, Eur. J. Med. Chem. 76 (2014) 494–505. https://doi.org/10.1016/j.ejmech.2014.01.030.
[15] A. Kluczyk, T. Popek, T. Kiyota, P. de Macedo, P. Stefanowicz, C. Lazar, Y. Konishi, Drug evolution: p-aminobenzoic acid as a building block, Curr. Med. Chem. 9 (2002) 1871–1892. https://doi.org/10.2174/092986702336887 2.
[16] R.G. Finch, D. Greenwood, R.J. Whitley, S.R. Norrby, Antibiotic and chemotherapy e-book, ninth ed. ed., Elsevier Health Sciences, Philadelphia, USA, 2010.
[17] M.C. Davis, S.G. Franzblau, A.R. Martin, Syntheses and evaluation of benzodiazaborine compounds against M. tuberculosis $H_{37}R_v$ in vitro, Bioorg. Med. Chem. Lett 8 (1998) 843–846. https://doi.org/10.1016/S0960-894X(98)00126-7.
[18] S. Lee, S. Oh, G.M. Park, T.S. Kim, J.S. Ryu, H.K. Choi, Antimalarial activity of thiophenyl- and benzenesulfonyl-dihydroartemisinin, Kor. J. Parasitol. 43 (2005) 123–126. https://doi.org/10.3347/kjp.2005.43.3.123.
[19] T.R. Pinheiro, R.A. Yunes, S.N. López, C.B. Santecchia, S.A.S. Zacchino, V. Cechinel Filho, In vitro antifungal evaluation and studies on the mode of action of xanthoxyline derivatives, Arzneimittelforschung 49 (1999) 1039–1043. https://doi.org/10.1055/s-0031-1300548.
[20] L. Garuti, M. Roberti, C. Cermelli, Synthesis and antiviral activity of some N-benzenesulphonylbenzimidazoles, Bioorg. Med. Chem. Lett 9 (1999) 2525–2530. https://doi.org/10.1016/S0960-894X(99)00429-1.
[21] L. Garuti, M. Roberti, T. Rossi, C. Cermelli, M. Portolani, M. Malagoli, M. Castelli, Synthesis, antiviral and antiproliferative activity of some N-benzenesulphonyl-2-(2- or 3-pyridylethyl)-benzimidazoles, Anti Cancer Drug Des. 13 (1998) 397–406.
[22] P.S. Charifson, J.P. Bowen, S.D. Wyrick, A.J. Hoffman, M. Cory, A.T. McPhail, R.B. Mailman, Conformational Analysis and Molecular Modeling of 1-Phenyl-,

4-Phenyl-, and l-Benzyl-l,2,3,4-tetrahydroisoquinolines as D_1 Dopamine Receptor Ligands, J. Med. Chem. 32 (1989) 2050–2058. https://doi.org/10.1021/jm00129a006.
[23] JME Molecular Editor Applet Allowing Creation or Editing of Molecules, Available Online: http://www.molinspiration.com/jme.
[24] T. Sander, J. Freyss, M. von Korff, J.R. Reich, C. Rufener, OSIRIS, an entirely in-house developed drug discovery informatics system, J. Chem. Inf. Model. 49 (2009) 232–246. https://doi.org/10.1021/ci800305f.
[25] D.F. Veber, S.R. Johnson, H.Y. Cheng, B.R. Smith, K.W. Ward, K.D. Kopple, Molecular properties that influence the oral bioavailability of drug candidates, J. Med. Chem. 45 (2002) 2615–2623. https://doi.org/10.1021/jm020017n.
[26] J.R. Denton, One-pot desulfonylative alkylation of N-sulfonyl azacycles using alkoxides generated by phase-transfer catalysis, Synthesis, 2010, pp. 775–782, 2010, https://doi.org/10.1055/s-0029-1218627.
[27] K. Abdireimov, N. Mukhamedov, M.Z. Aiymbetov, K.M. Shakhidoyatov, Benzazoles. 3*. Synthesis and arylsulfonylation of 2-substituted benzimidazoles, Chem. Heterocycl. Comp. 46 (2010) 941–946.
[28] K. Tyler, D. Engman, The life cycle of Trypanosoma cruzi revisited, Int. J. Parasitol. 31 (2001) 472–481. https://doi.org/10.1016/S0020-7519(01)00153-9.
[29] M.L. Sykes, V.M. Avery, Approaches to protozoan drug discovery: phenotypic screening: Miniperspectives series on phenotypic screening for antiinfective targets, J. Med. Chem. 56 (2013) 7727–7740. https://doi.org/10.1021/jm4004279.
[30] B. Muro, F. Reviriego, P. Navarro, C. Marín, I. Ramírez-Macías, M.J. Rosales, M. Sánchez-Moreno, V.J. Arán, New perspectives on the synthesis and anti-chagasic activity of 3-alkoxy-1-alkyl-5-nitroindazoles, Eur. J. Med. Chem. 74 (2014) 124–134. https://doi.org/10.1016/j.ejmech.2013.12.025.
[31] I. Ramírez-Macías, C. Marín, H. Es-Samti, A. Fernández, J.J. Guardia, H. Zentar, A. Agil, R. Chahboun, E. Alvarez-Manzaneda, M. Sánchez-Moreno, Taiwaniaquinoid and abietane quinone derivatives with trypanocidal activity against T. cruzi and Leishmania spp, Parasitol. Int. 61 (2012) 405–413. https://doi.org/10.1016/j.parint.2012.02.001v.
[32] I. Ramírez-Macías, C.R. Maldonado, C. Marín, F. Olmo, R. Gutiérrez-Sánchez, M.J. Rosales, M. Quirós, J.M. Salas, M. Sánchez-Moreno, In vitro anti-leishmania evaluation of nickel complexes with a triazolopyrimidine derivative against Leishmania infantum and Leishmania braziliensis, J. Inorg. Biochem. 112 (2012) 1–9. https://doi.org/10.1016/j.jinorgbio.2012.02.025.
[33] M.A. Bryan, S.E. Guyach, K.A. Norris, Specific humoral immunity versus polyclonal B Cell activation in trypanosoma cruzi infection of susceptible and resistant mice, PLoS Neglected Trop. Dis. 4 (2010). https://doi.org/10.1371/journal.pntd.0000733.
[34] F. Bringaud, L. Rivière, V. Coustou, Energy metabolism of trypanosomatids: adaptation to available carbon sources, Mol. Biochem. Parasitol. 149 (2006) 1–9. https://doi.org/10.1016/j.molbiopara.2006.03.017.
[35] J. Turrens, More differences in energy metabolism between Trypanosomatidae, Parasitol. Today 15 (1999) 346.
[36] C. Fernández-Becerra, M. Sánchez-Moreno, A. Osuna, F. Opperdoes, Comparative aspects of energy metabolism in plant trypanosomatids, J. Eukaryot. Microbiol. 44 (1997) 523–529. https://doi.org/10.1111/j.1550-7408.1997.tb05734.x.
[37] A.P. Bento, A. Gaulton, A. Hersey, L.J. Bellis, J. Chambers, M. Davies, F.A. Krüger, Y. Light, L. Mak, S. McGlinchey, The ChEMBL bioactivity database: an update, Nucleic Acids Res. 42 (2014) D1083–D1090. https://doi.org/10.1093/nar/gkt1031.
[38] UniProt Consortium - UniProt, the universal protein knowledgebase, Nucleic Acids Res. 46 (2018) 2699. https://doi.org/10.1093/nar/gkw1099.
[39] J. Martinez-Oyanedel, I.W. McNae, M.W. Nowicki, J.W. Keillor, P.A. Michels, L.A. Fothergill-Gilmore, M.D. Walkinshaw, The first crystal structure of phosphofructokinase from a eukaryote: Trypanosoma brucei, J. Mol. Biol. 366 (2007) 1185–1198. https://doi.org/10.1016/j.jmb.2006.10.019.
[40] I.W. McNae, J. Martinez-Oyanedel, J.W. Keillor, P.A. Michels, L.A. Fothergill-Gilmore, M.D. Walkinshaw, The crystal structure of ATP-bound phosphofructokinase from Trypanosoma brucei reveals conformational transitions different from those of other phosphofructokinases, J. Mol. Biol. 385 (2009) 1519–1533. https://doi.org/10.1016/j.jmb.2008.11.047.
[41] M.-A. Albert, J.R. Haanstra, V. Hannaert, J. Van Roy, F.R. Opperdoes, B.M. Bakker, P.A. Michels, Experimental and in silico analyses of glycolytic flux control in bloodstream form Trypanosoma brucei, J. Biol. Chem. 280 (2005) 28306–28315. https://doi.org/10.1074/jbc.M502403200.
[42] K.R. Brimacombe, M.J. Walsh, L. Liu, M.G. Vásquez-Valdivieso, H.P. Morgan, I. McNae, L.A. Fothergill-Gilmore, P.A. Michels, D.S. Auld, A. Simeonov, Identification of ML251, a potent inhibitor of T. brucei and T. cruzi phosphofructokinase, ACS Med. Chem. Lett. 5 (2013) 12–17. https://doi.org/10.1021/ml400259d.
[43] C. Merritt, L.E. Silva, A.L. Tanner, K. Stuart, M.P. Pollastri, Kinases as druggable targets in trypanosomatid protozoan parasites, Chem. Rev. 114 (2014) 11280–11304. https://doi.org/10.1021/cr500197d.
[44] Fred3.0.0 OpenEye Scientific Software, Santa Fe, NM http://www.eyesopen.com.
[45] A. Fiser, A. Šali, Modeller: generation and refinement of homology-based protein structure models, in: C.W. Carter Jr., R.M. Sweet (Eds.), Methods Enzymol., Elsevier, Ámsterdam, 2003, pp. 461–491.
[46] D.A. Case, J.T. Berryman, R.M. Betz, D.S. Cerutti, I.T.E. Cheatham, T.A. Darden, R.E. Duke, T.J. Giese, H. Gohlke, A.W. Goetz, N. Homeyer, S. Izadi, P. Janowski, J. Kaus, A. Kovalenko, T.S. Lee, S. LeGrand, P. Li, T. Luchko, R. Luo, B. Madej, K.M. Merz, G. Monard, P. Needham, H. Nguyen, H.T. Nguyen, I. Omelyan, A. Onufriev, D.R. Roe, A.E. Roitberg, R. Salomon-Ferrer, C. Simmerling, W. Smith, J. Swails, R.C. Walker, J. Wang, R.M. Wolf, X. Wu, D.M. York, P.A. Kollman, AMBER 2016, University of California, San Francisco, 2016.
[47] J.A. Maier, C. Martinez, K. Kasavajhala, L. Wickstrom, K.E. Hauser, C. Simmerling, ff14SB: improving the accuracy of protein side chain and backbone parameters from ff99SB, J. Chem. Theor. Comput. 11 (2015) 3696–3713. https://doi.org/10.1021/acs.jctc.5b00255.
[48] OpenEye Scientific Software, in, OpenEye Scientific Software.
[49] Omega.2.4.3 - OpenEye Scientific Software, Santa Fe, NM http://www.eyesopen.com.
[50] P.C. Hawkins, A. Nicholls, Conformer generation with OMEGA: learning from the data set and the analysis of failures, J. Chem. Inf. Model. 52 (2012) 2919–2936. https://doi.org/10.1021/ci300314k.
[51] M. McGann, FRED pose prediction and virtual screening accuracy, J. Chem. Inf. Model. 51 (2011) 578–596. https://doi.org/10.1021/ci100436p.
[52] M. McGann, FRED and HYBRID docking performance on standardized datasets, J. Comput. Aided Mol. Des. 26 (2012) 897–906.
[53] VIDA.4.3.0 - OpenEye Scientific Software, Santa Fe, NM http://www.eyesopen.com.
[54] R.A. Laskowski, M.B. Swindells, LigPlot+: multiple ligand–protein interaction diagrams for drug discovery, J. Chem. Inf. Model. 51 (2011) 2778–2786. https://10.1021/ci200227u.
[55] B.R. Miller III, T.D. McGee Jr., J.M. Swails, N. Homeyer, H. Gohlke, A.E. Roitberg, MMPBSA. py: an efficient program for end-state free energy calculations, J. Chem. Theor. Comput. 8 (2012) 3314–3321. https://doi.org/10.1021/ct300418h.
[56] P.A. Kollman, I. Massova, C. Reyes, B. Kuhn, S. Huo, L. Chong, M. Lee, T. Lee, Y. Duan, W. Wang, Calculating structures and free energies of complex molecules: combining molecular mechanics and continuum models, Acc. Chem. Res. 33 (2000) 889–897. https://doi.org/10.1021/ar000033j.